



# A nanometric temperature sensor based on plasmonic waveguide with an ethanol-sealed rectangular cavity

Tiesheng Wu<sup>a</sup>, Yumin Liu<sup>a,b,\*</sup>, Zhongyuan Yu<sup>a</sup>, Han Ye<sup>a</sup>, Yiwei Peng<sup>a</sup>, Changgan Shu<sup>a</sup>, Chuanghua Yang<sup>a</sup>, Wen Zhang<sup>a</sup>, Huifang He<sup>a</sup>

<sup>a</sup> State Key Laboratory of Information Photonics and Optical Communications, Beijing University of Posts and Telecommunications, Beijing 100876, China

<sup>b</sup> State Key Laboratory of Integrated Optoelectronics, Institute of Semiconductors, Chinese Academy of Sciences, Beijing 100083, China

## ARTICLE INFO

### Article history:

Received 24 June 2014

Received in revised form

14 November 2014

Accepted 19 November 2014

Available online 21 November 2014

### Keywords:

Surface plasmons

Optical sensing and sensors

Temperature

Optical resonators

## ABSTRACT

A surface plasmon polaritons (SPPs) temperature sensor which consists of two metal–insulator–metal (MIM) waveguides coupled to each other by an ethanol-sealed rectangular cavity is proposed. The transmission characteristics of the nanodevice are theoretically analyzed and numerically simulated by two-dimension finite difference time domain (FDTD) method. The temperature sensing characteristics of the SPPs waveguide sensor are systematically analyzed by investigating the transmission spectra. The results indicate that the position of the transmission peak wavelengths has a linear relationship with the ambient temperature. The temperature sensitivity increases with the increase of the cavity length and decrease of the cavity height. The temperature sensitivity of the nanometric sensor can reach as high as  $-0.65 \text{ nm/}^\circ\text{C}$ . It could be utilized to develop ultracompact temperature sensor for high integration.

© 2014 Elsevier B.V. All rights reserved.

## 1. Introduction

Temperature sensor means able to sense temperature and convert it into an output signal that can be measured. Temperature sensor is a core part of the temperature measuring instruments that permeate our daily lives. Conventional electronic-based thermometers are the most popular sensing devices due to their technological maturity [1]. There are four major types of electronic-based temperature sensors: thermocouple, thermistor, resistance temperature detector (RTD), and integrated circuit (IC) temperature sensor. However, electromagnetic interference is identified as one of the main limiting factors that restrict their use. An optoelectronic temperature sensor is an alternative approach which offers various advantages over conventional methods, including electromagnetic interference immunity, compactness, large temperature range, high sensitivity, reliability and multiple spatially separated sensors configured as a sensing network [1,2]. In the past few decades, fiber optic temperature sensors are widely studied and used, such as fiber Bragg gratings, long-period fiber gratings, varieties of optical fiber interferometers and other interesting structures [3–9].

In recent years, plasmonic temperature sensors have been proposed and demonstrated due to continuous improvement in nanofabrication and nanocharacterization capabilities. Both SPPs and localized surface plasmon resonances (LSPRs) exhibit very interesting properties for sensing application due to their high degree of tenability and their susceptibility to the dielectric properties of the surrounding environment and structures [10–15]. Some plasmonic temperature sensing approaches have been demonstrated, for example, Peng et al. demonstrated a temperature sensor based on LSPRs supported by photonic crystal fiber with a temperature sensitivity as high as  $720 \text{ pm/}^\circ\text{C}$  [16], Sahin et al. demonstrated a three-interface LSPRs geometry with the “angular interrogation” approach [17], and the well-known Kretschmann’s analysis [18,19]. As a matter of fact, these reported LSPRs temperature sensors are difficult to integrate into chips.

In the quest of integration and compactness, in this paper, a novel SPPs temperature sensor based on MIM waveguide coupled with an ethanol-sealed rectangular cavity is proposed. The 2D FDTD method with perfectly matched layer (PML) is employed to simulate and research its sensing characteristics. A PML is an artificial absorbing layer for wave equations, commonly used to truncate computational regions in numerical methods to simulate problems with open boundaries. It is designed so that waves incident upon the PML from a non-PML medium do not reflect at the interface. This property allows the PML to strongly absorb outgoing waves from the interior of a computational region without

\* Corresponding author at: State Key Laboratory of Information Photonics and Optical Communications, Beijing University of Posts and Telecommunications, Beijing 100876, China.

E-mail address: [microluiyumin@hotmail.com](mailto:microluiyumin@hotmail.com) (Y. Liu).

reflecting them back into the interior. The relationship between the resonance peaks in the transmission spectra and ambient temperature is analyzed. Additionally, the structural parameters of the sensor impact on sensitivity are analyzed to optimize the performance. At present, there is no other research group reported temperature sensing based SPPs waveguide. In our previous work [13,15], we proposed using SPPs waveguide for temperature sensing, but this is the first time we systematically research SPPs temperature sensor. Although we only do some numerical analysis about SPPs temperature sensor, this work promotes the application scope of SPPs waveguide.

## 2. Theory model and sensing principle

The proposed SPPs temperature sensor is schematically shown in Fig. 1(a), which consists of two MIM waveguides and a rectangular cavity. The nanocavity is filled with ethanol and it can be achieved by capillary attraction [4]. Note that in this structure, the ethanol is sealed in the cavity by a dielectric material which locates on the upper surface of the silver film, and the dielectric material is not depicted in Fig. 1(a). The yellow, green and purple parts denote Ag, ethanol and quartz substrate, respectively. The slits parts denote Air. One way to fabricate this structure is by the focused ion beam (Strata FIB201, FEI Company) on a 100 nm thick silver film that is sputtered on a quartz substrate, and the other way is by depositing 100 nm silver and then etching silver film, which are described in detail in Refs. [10–12]. The light can be coupled into the sensor by nano-fiber and the output light can be detected by JY Confocal Raman Microscopy [13]. To simplify the problem and to save some calculation time and reduce the computational burden, 2D simulation is performed in this paper. The 2D model is shown in Fig. 1(b),  $d$  are the widths of the slits,  $w$  are the coupling lengths between the waveguides and the rectangular cavity,  $L$  and  $H$  are the length and the height of the rectangular cavity, and the thickness of Ag film of the MIM waveguide is set to be 100 nm, respectively.

As is well known, the dispersion equation of the fundamental TM mode in the MIM structure (shown in the inset of Fig. 2) can be written as [20–22]

$$\varepsilon_{in}k_{z2} + \varepsilon_m k_{z1} \coth\left(-\frac{ik_{z1}d}{2}\right) = 0, \quad (1)$$

with  $K_{z1}$  and  $K_{z2}$  are defined by momentum conservations

$$K_{z1}^2 = \varepsilon_{in}K_0^2 - \beta^2, \quad (2)$$

$$K_{z2}^2 = \varepsilon_m K_0^2 - \beta^2, \quad (3)$$

where  $\varepsilon_{in}(\varepsilon_{in} = n^2)$ ,  $\varepsilon_m$  are the dielectric constants of the insulator and the metal, respectively,  $\beta$  is the propagation constant of the SPPs and  $k_0 = 2\pi/\lambda$  is the free-space wave vector. The complex

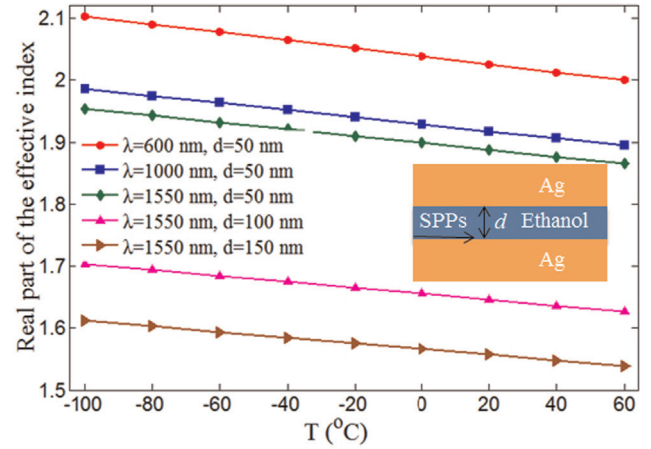


Fig. 2. Real part of the effective index  $n_{eff}$  versus the ambient temperature in an Ag–ethanol–Ag waveguide structure for different incident wavelengths and different waveguide widths.

refractive index of Ag as a function of  $\lambda$  is taken from Palik [23]. The refractive index of ethanol can be defined as [4,13]

$$n = 1.36048 - 3.94 \times 10^{-4}(T - T_0), \quad (4)$$

where  $T_0$  is the room temperature with a value of 20 °C,  $T$  is the ambient temperature. The reason why we choose ethanol is that it has a relatively high thermo-optic coefficient. The thermo-optic coefficient of quartz is about  $\alpha = 8.6 \times 10^{-6}$  [4], and the thermo-optic coefficient of Ag is approximately equal to  $9.3 \times 10^{-6}$  [24]. Because the thermo-optic coefficients of quartz and Ag are two orders of magnitude smaller than the thermo-optic coefficient of ethanol, in the analysis of the temperature sensing, the impact of temperature variability on the refractive indices of quartz and Ag can be ignored. The real part of the effective index  $n_{eff} = \text{real}(\beta/k_0)$  of the SPPs waveguide with Ag–ethanol–Ag structure as a function of the ambient temperature at different wavelengths and at different slit widths is shown in Fig. 2. Obviously, the effective refractive index decreases with increasing the temperature, the relationship of them should be expressed in a linear function within the range of  $-100$ – $60$  °C at all wavelengths. According to the temporal coupled-mode theory, the transmittance  $T_1$  of the sensor can be described as [20,25,26]

$$T_1 = \frac{\Gamma^2}{(\Delta\omega)^2 + (\Gamma_0 + \Gamma)^2}, \quad (5)$$

where  $\Delta\omega = \omega - \omega_0$ ,  $\Gamma_0 = 1/\tau_0$ ,  $\Gamma = 1/\tau_- + 1/\tau_+$ , and  $1/\tau_0$  is the decay rate due to the intrinsic loss of the SPPs,  $1/\tau_-$  and  $1/\tau_+$  are the power coupling rates of decay into the bus and the receive waveguides, respectively. In our structure,  $1/\tau_- = 1/\tau_+$ . The  $\Delta\omega_{FWHM}$  can be calculated from the rectangular cavity parameters by equating the right hand side of Eq. (5) to half the maximum,

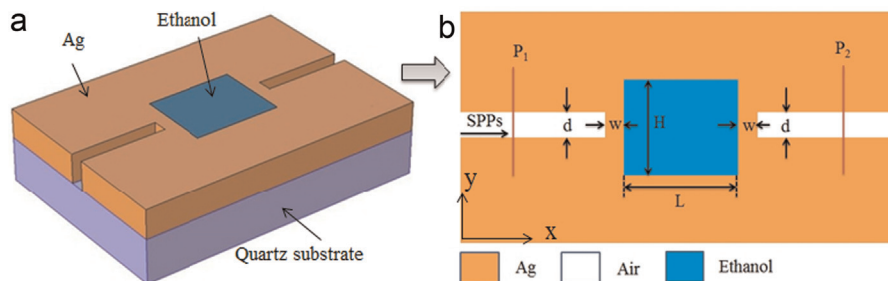


Fig. 1. Structure schematic of the nanoscale temperature sensor. (a) Three-dimensional structure. (b) Two-dimensional structure. (For interpretation of the references to color in this figure the reader is referred to the web version of this article.)

$$\Delta\omega_{FWHM} = 2(I_0 + \Gamma). \quad (6)$$

In the rectangular cavity, the accumulated phase shift per round trip for the SPPs is

$$\Phi = 4\pi \operatorname{Re}(n_{\text{eff}})L/\lambda + 2\varphi, \quad (7)$$

where  $\varphi$  is the phase shift of the SPPs reflected off at the end of the rectangular cavity, and  $n_{\text{eff}}$  is the effective refractive index of the SPPs. At the resonant wavelength  $\lambda_0$ , the incident power can pass through and results in a peak in the transmission spectra, and the resonant condition is

$$\Phi = 4\pi \operatorname{Re}(n_{\text{eff}})L/\lambda_0 + 2\varphi = 2m\pi, \quad (8)$$

where  $m$  is an integer. According to Eq. (8), the resonant wavelength can be described as

$$\lambda_0 = 2 \operatorname{Re}(n_{\text{eff}})L/(m - \varphi/\pi). \quad (9)$$

Only those wavelengths satisfy the Eq. (9) can be transported efficiently, while others are stopped. Based on Eq. (9), the resonant wavelength of  $\lambda_0$  is proportional to the effective refractive index of the SPPs, and while the effective refractive index is inversely proportional to temperature as shown in Fig. 2, therefore, the resonance wavelength is inversely proportional to temperature and the proportionality coefficient (temperature sensitivity) is

$$\frac{d\lambda_0}{dT} = 2 \frac{d(\operatorname{Re}(n_{\text{eff}}))}{dT} L/(m - \varphi/\pi). \quad (10)$$

The temperature measurement capability of the plasmonic waveguide with an ethanol-sealed rectangular cavity is mainly derived from the refractive index sensitivity. With the temperature increasing, the refractive index of ethanol decreases rapidly due to the thermo-optic effect, resulting in the effective refractive index variation and the resonant wavelengths shift. In order to investigate the temperature sensing characteristics of the SPPs waveguide with an ethanol-sealed rectangular cavity, its transmission spectra are simulated by using FDTD method with PMLs. In the simulations, all external boundaries are set as PMLs, and the fundamental TM mode of the MIM waveguide is excited by a mode source. The mode source is used to inject a guided mode into the simulation region. The geometry of the mode source (i.e. center location, and span) is used to compute the guide modes for the structure. In 3D simulations, the modes are computed across a plane, while in 2D they are computed across a line. In this paper, the mode source is used to inject the fundamental TM mode of the plasmonic waveguide into the simulation region. The grid sizes in the  $x$  and  $y$  directions are set to be  $\Delta x = \Delta y = 5$  nm and the time step, derived by Courant

condition [27,28]

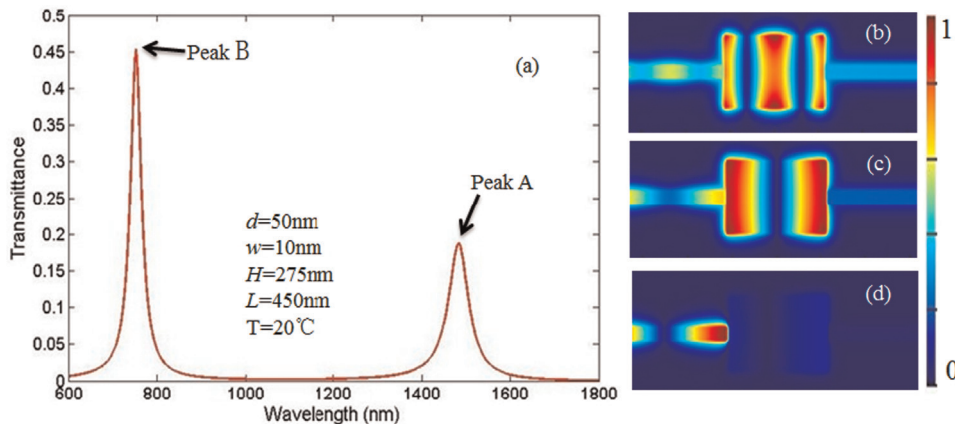
$$\Delta t = \frac{0.95}{c} \sqrt{(\Delta x)^{-2} + (\Delta y)^{-2}}, \quad (11)$$

where  $c$  is denotes the speed of light in free space. Two power monitors  $P_1$  and  $P_2$  are set to detect the incident power  $P_{\text{in}}$  (without the resonant cavity for reference) and the transmission power  $P_{\text{out}}$  (with the resonant cavity). The distance between  $P_1$  and  $P_2$  is set to be 1400 nm. The transmittance of the sensor is defined as  $T_1 = P_{\text{out}}/P_{\text{in}}$  [21]. When those wavelengths satisfy Eq. (9), the maximum transmittance will be obtained.

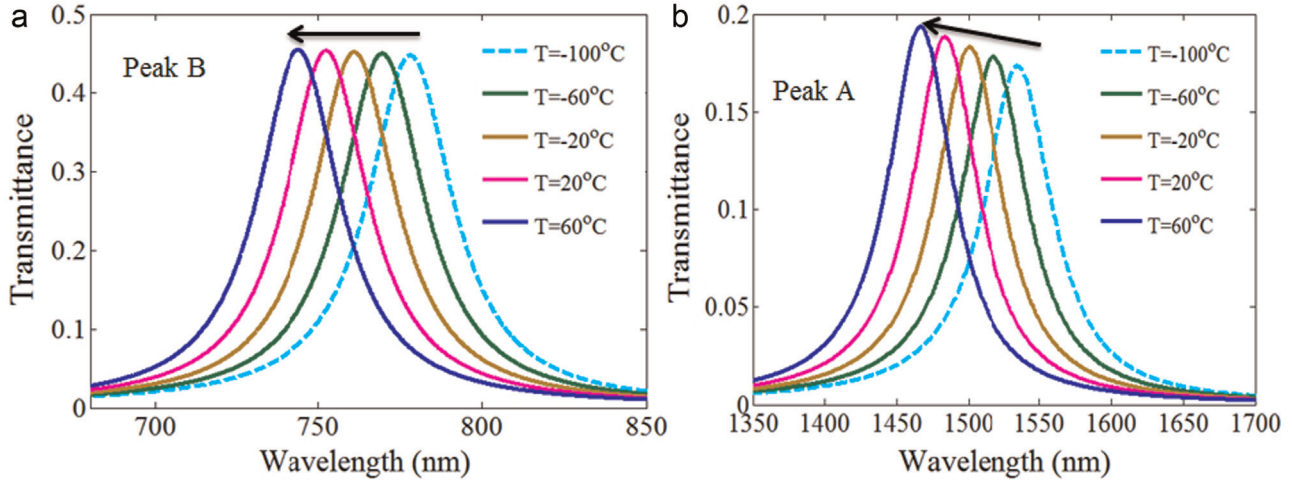
### 3. Results and discussions

Fig. 3(a) shows the transmission spectra of the structure when temperature  $T=20^\circ\text{C}$ . The widths of the slits  $d$  are set to be 50 nm, the coupling lengths  $w$  between the SPPs waveguides and the rectangular cavity are set to be 10 nm, the length  $L$  and the height  $H$  of the cavity are set to be 450 nm, 275 nm, respectively. In Fig. 3(a), it is shown that there are two transmission peaks occur at the resonant wavelengths of 1483.4 nm and 752.3 nm, corresponding to the peak A and the peak B of the transmission spectra. The transmission at the peak A is close to 19%, and the transmission at the peak B is about 45%, the optical loss of the peak A is bigger than that of the peak B. The full width at half maximum (FWHM) is 55.6 nm at the peak A and 31.1 nm at the peak B. Fig. 3(b)–(d) shows the contour profiles of the fields  $|H_z|$  at different wavelengths. The field  $|H_z|$  distributions in Fig. 3(b) and (c) correspond to the resonant peak wavelengths at the peak B and the peak A, respectively. It is obvious that when the resonance condition of Eq. (8) is satisfied, the maximum transmission of the SPPs can be obtained. In Fig. 3(d), the wavelength  $\lambda$  is 1800 nm, the field  $|H_z|$  distribution in the rectangular cavity is very weak, and there is almost no magnetic field in the right-side slit, indicating that the transmission of the SPPs is forbidden in this case [13,29].

Next, we move on to study the temperature sensing characteristics of the structure by analyzing the transmission spectra. The parameters of the structure are set to be  $d=50$  nm,  $w=10$  nm,  $L=450$  nm, and  $H=275$  nm. Fig. 4(a) and (b) shows the transmission spectra of the sensor for different temperature from  $-100^\circ\text{C}$  to  $60^\circ\text{C}$  with step of  $20^\circ\text{C}$ . As the temperature increases, the transmission spectra exhibit blue shift. According to Eqs. (2) and (9), the refractive index of ethanol decreases with increasing the temperature, and the transmission peak wavelength is related to the effective refractive index of the SPPs in the nanocavity, while the effective refractive index of the SPPs is



**Fig. 3.** (a) Transmission spectra of the sensor when  $T=20^\circ\text{C}$ , with  $d=50$  nm,  $w=10$  nm,  $L=450$  nm,  $H=275$  nm. The contour profiles of field  $H_z$  of the sensor at different wavelengths of (b)  $\lambda=752.3$  nm, (c)  $\lambda=1483.4$  nm, and (d)  $\lambda=1800$  nm.



**Fig. 4.** Transmission spectra of the sensor for different temperature with  $d=50$  nm,  $w=10$  nm,  $L=450$  nm, and  $H=275$  nm. (a) Corresponding to the peak B. (b) Corresponding to the peak A.

inversely proportional to temperature as shown in Fig. 2, therefore, the transmission spectra exhibit shift when temperature varies, the FDTD simulations agree with theoretical analysis.

Fig. 5(a) depicts the two peaks of the transmission spectra as a function of the temperature. The two peaks have good linear relationship with the temperature. Both of the peaks shift to shorter wavelengths with increasing the temperature. Obviously, according to the linear relationship between the peaks of the transmission spectra and the temperature, we can obtain the temperature from detecting one peak wavelength of the transmission spectra. Fig. 5(b) presents the simulation data of the peaks wavelengths shift as a function of the temperature. The temperature is varied from  $-100$  °C to  $60$  °C, the shift of the peak A equals to  $-68.20$  nm, and the shift of the peak B equals to  $-34.23$  nm. The temperature sensitivity is defined as  $\Delta\lambda/\Delta T$  (nm/°C), resulting in  $-0.43$  nm/°C for the peak A, and  $-0.21$  nm/°C for the peak B, respectively. The temperature sensitivity of peak A is about twice that of the peak B. However, there is an unfavorable factor that the optical loss of the peak A is greater. Considering the melting and the boiling point of ethanol are  $-114$  °C and  $78.4$  °C, respectively, thus the measurement of this technique has to be within this range. In other words, the SPPs sensor which filled with ethanol in the rectangle cavity is suitable for low temperature measurement.

Finally, the parameters of the structure impact on the sensing sensitivity and the optical loss are analyzed in order to improve

the performance. According to Eq. (9), the resonant wavelength is proportional to the length of cavity  $L$ , the resonance wavelength increases with increasing the cavity length. Fig. 6(b) shows the transmission spectra of the SPPs for different cavity lengths with  $d=50$  nm,  $w=10$  nm,  $H=275$  nm, and  $T=20$  °C. The transmission peaks exhibit linearly red shift as the cavity length increase. According to Eq. (10), temperature sensitivity is proportional to the length of cavity  $L$ , the temperature sensitivity increases with increasing cavity length. Fig. 6(a) demonstrates the temperature sensitivity as a function of the cavity length  $L$  with different  $d$  and different  $w$ . As can be seen from Fig. 6(a), the simulation data agree well with the theoretical analysis. The widths of the slits  $d$  and the coupling lengths  $w$  have little effect on the temperature sensitivity. The cavity length is a double-edged sword, the temperature sensitivity is improved with increasing the cavity length, and however, the disadvantage introduced by increasing the cavity length is the additional optical loss. The transmission spectra of the structure are calculated by varying  $w$  and the results are displayed in Fig. 6(c). The parameters are set to be  $d=50$  nm,  $L=450$  nm,  $H=275$  nm, and  $T=20$  °C, respectively. When  $w=0$  nm, the peak A exhibits a broadband transmission spectra with a FWHM of about  $\Delta\lambda_{FWHM} = 560.4$  nm. While the FWHM of peak B is about  $50.6$  nm. The FWHM decreases with increasing  $w$ . However, the optical loss dramatically increases with increasing the coupling lengths  $w$ . This is because a large coupling distance

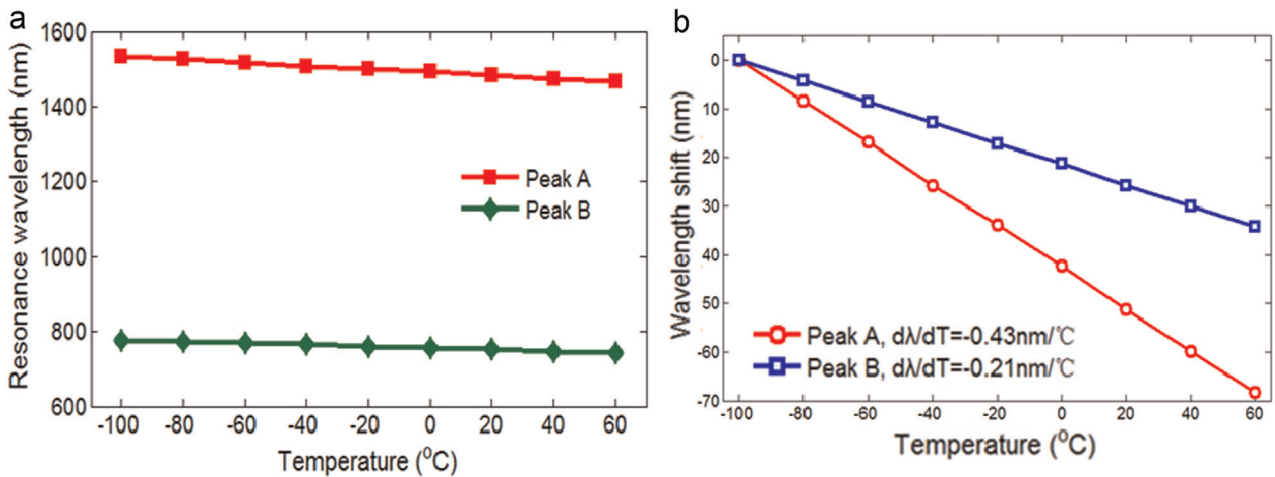


**Fig. 5.** (a) The resonance wavelengths of the structure versus the temperature. (b) The shift of the resonance wavelength as a function of the temperature.



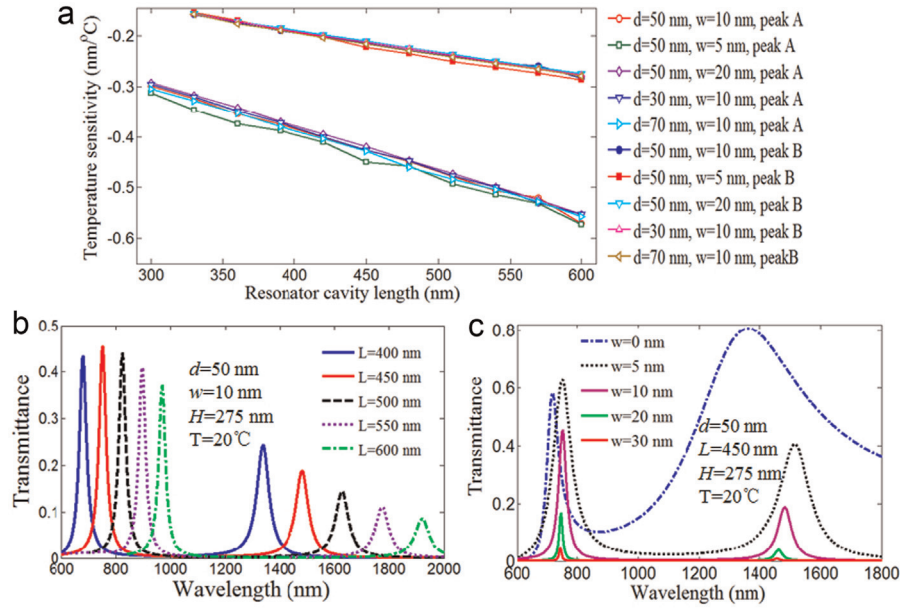


**Fig. 6.** (a) The temperature sensitivity versus cavity length of  $L$ . (b) Transmission spectra of the sensor for different cavity lengths with  $d=50$  nm,  $w=10$  nm,  $H=275$  nm, and  $T=20$  °C. (c) Transmission spectra of the sensor for different coupling lengths between the wavelengths and the rectangular cavity with  $d=50$  nm,  $L=450$  nm,  $H=275$  nm, and  $T=20$  °C.

would result in a small coupling strength.

Because of the temperature sensitivity of the peak A is much higher than that of the peak B, we want to use the peak A for temperature sensing. Fig. 7(a) shows the transmission spectra of the structure for the peak A with different cavity heights. The parameters of the structure are set to be  $d=50$  nm,  $w=10$  nm,  $L=450$  nm, and the temperature is set to be  $T=20$  °C. As can be seen in Fig. 7(a), the peak A exhibits red shift with decreasing the cavity height and while the optical loss decreases. Fig. 7(b) shows the temperature sensitivity of the peak A versus the cavity height of  $H$  with different cavity lengths. The cavity height increases from 50 nm to 450 nm, the parameters of the structure are set to be  $d=50$  nm,  $w=10$  nm, and  $L$  are given 360 nm, 450 nm, 540 nm, respectively. The temperature sensitivity of the peak A increases with decreasing the cavity height. Because of the temperature sensitivity of the sensor is mainly derived from the refractive index sensitivity. As seen in Fig. 2, with the same amount of temperature change, the change of the effective refractive index of the

SPPs mode in the rectangular cavity will decrease when the cavity height increase. Decreasing the height not only can improve the temperature sensitivity, but also will decrease the optical loss. Therefore, we can improve the sensitivity of the plasmonic temperature sensor by means of increased the cavity length  $L$  and/or decreased the cavity height  $H$ . When the parameters of the structure are set to be  $d=50$  nm,  $w=10$  nm,  $L=540$  nm, and  $H=50$  nm, respectively, the temperature sensitivity of the peak A is as high as  $-0.65$  nm/°C. Higher temperature sensitivity can be realized by filled some liquid having a higher thermo-optic coefficient into the nanocavity. To the best of our knowledge, the temperature sensitivity of the SPPs temperature sensor is not inferior to the fiber optic sensor [1–3,5–8]. In practical applications, we can use lithium niobate instead of ethanol for making of all solid-state devices. Additionally, this structure can be used as a refractive index sensor or biosensor; since the wavelengths of the SPPs corresponded to the transmission peaks are allowed to transport efficiently, while others are forbidden [29], so we

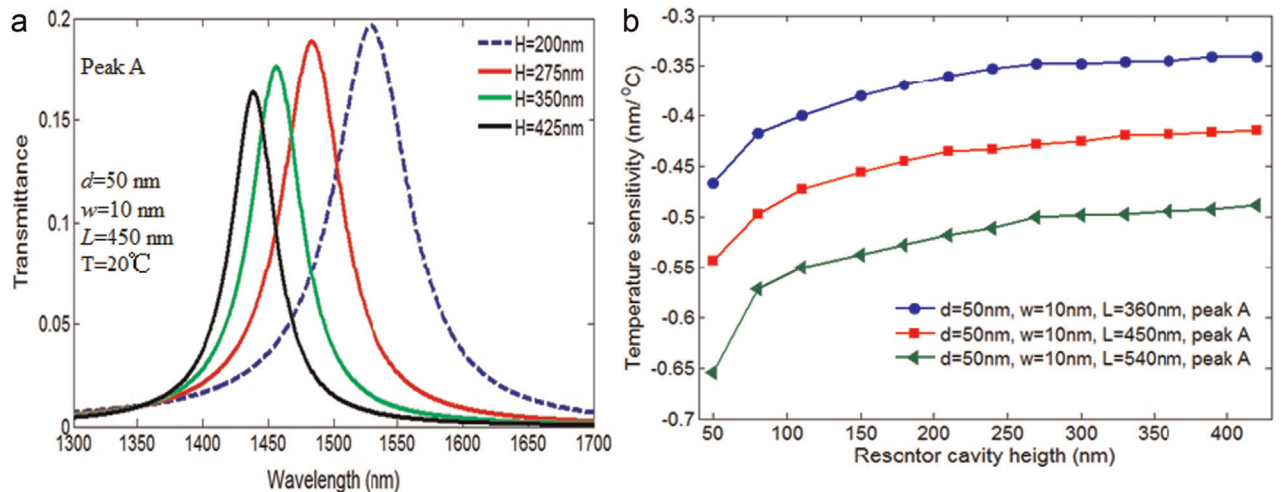


**Fig. 7.** (a) Transmission spectra of the sensor for peak A with different cavity heights,  $d=50$  nm,  $w=10$  nm,  $L=450$  nm, and  $T=20$  °C. (b) The temperature sensitivity of the peak A versus cavity height of  $H$  with  $d=50$  nm,  $w=10$  nm.

proposed structure can be used as a tunable SPPs filter by controlling the temperature.

#### 4. Conclusion

In summary, we have proposed a SPPs waveguide structure coupled by an ethanol-sealed rectangle cavity for temperature sensing. The temperature measurement is attributed to the resonance peaks linearly shift resulting from the thermo-optic effect of ethanol. The temperature sensitivity is related to the length and the height of the nanocavity, and the thermo-optic coefficient of sealed liquid. A temperature sensitivity of  $-0.65 \text{ nm}/^\circ\text{C}$  has been obtained theoretically by 2D-FDTD simulations. The ultracompact structure together with planar waveguide configuration makes it easy to integrate to chips. In addition, the device can be used as a tunable SPPs band-pass filter by controlling the temperature. The results have guiding significance for designing nanoscale devices.

#### Acknowledgments

The work was supported by the National Natural Science Foundation of China (61275201, 61372037), Beijing Excellent Ph.D. Thesis Guidance Foundation (Grant no. 20131001301), the Fund of State Key Laboratory of Information Photonics and Optical Communications (Beijing University of Posts and Telecommunications), and the Opened Fund of the State Key Laboratory on Integrated Optoelectronics, Institute of Semiconductors, Chinese Academy of Sciences.

#### References

- [1] T.D. Vo, J.K. He, E. Magi, M.J. Collins, A.S. Clark, B.G. Ferguson, C.L. Xiong, B. J. Eggleton, Chalcogenide fiber-based distributed temperature sensor with sub-centimeter spatial resolution and enhanced accuracy, *Opt. Express* 22 (2) (2014) 1560–1568.
- [2] A.D. Kersey, M.A. Davis, H.J. Patrick, M. LeBlanc, K.P. Koo, C.G. Askins, M. A. Putnam, E.J. Friebele, Fiber grating sensors, *J. Lightwave Technol.* 15 (8) (1997) 1442–1463.
- [3] Y. Xue, Y.S. Yu, R. Yang, C. Wang, C. Chen, J.C. Guo, X.Y. Zhang, C.C. Zhu, H. B. Sun, Ultrasensitive temperature sensor based on an isopropanol-sealed optical microfiber taper, *Opt. Lett.* 38 (8) (2013) 1209–1211.
- [4] T.S. Wu, L. Wang, Z. Wang, A photonic crystal fiber temperature sensor based on Signac interferometer structure, *Chin. J. Lasers* 39 (11) (2012) 1114002.
- [5] S.J. Qiu, Y. Chen, F. Xu, Y.Q. Lu, Temperature sensor based on an isopropanol-sealed photonic crystal fiber in-line interferometer with enhanced refractive index sensitivity, *Opt. Lett.* 37 (5) (2012) 863–865.
- [6] P.F. Wang, M. Ding, L. Bo, C.Y. Guan, Y. Semenova, Q. Wu, G. Farrell, G. Brambilla, Fiber-tip high-temperature sensor based on multimode interference, *Opt. Lett.* 38 (22) (2013) 4617–4620.
- [7] D. Wu, T. Zhu, M. Liu, A high temperature sensor based on a peanut-shape structure Michelson interferometer, *Opt. Commun.* 285 (2012) 5085–5088.
- [8] F.C. Favero, R. Spittel, F. Just, J. Kobelke, M. Rothhardt, H. Bartelt, A miniature temperature high germanium doped PCF interferometer sensor, *Opt. Express* 21 (25) (2013) 30266–30274.
- [9] H.H. Lu, B. Sadani, G. Ulliac, C. Guyot, N. Courjal, M. Collet, F.I. Baida, M. P. Bernal, Integrated temperature sensor based on an enhanced pyroelectric photonic crystal, *Opt. Express* 21 (14) (2013) 16311–16318.
- [10] Q.Q. Cheng, T. Li, L. Li, S.M. Wang, S.N. Zhu, Mode division multiplexing in a polymer-loaded plasmonic planar waveguide, *Opt. Lett.* 39 (13) (2014) 3900–3902.
- [11] F. Beijnum, P.J. Veldhoven, E.J. Geluk, M.J.A. Dood, G.W. Hooft, M.P. Exter, Surface Plasmon Lasing Observed in Metal Hole Arrays, *Phys. Rev. Lett.* 110 (2013) 206802.
- [12] W.W. Zhang, C.L. Zhao, J.Y. Wang, J.S. Zhang, An experimental study of the plasmonic Talbot effect, *Opt. Express* 17 (22) (2009) 19757–19762.
- [13] T.S. Wu, Y.M. Liu, Z.Y. Yu, Y.W. Peng, C.G. Shu, H. Ye, The sensing characteristics of plasmonic waveguide with a ring resonator, *Opt. Express* 22 (7) (2014) 7669–7677.
- [14] K. Lodewijks, J. Ryken, W.V. Roy, G. Borghs, L. Lagae, P.V. Dorpe, Tuning the fano resonance between localized and propagating surface plasmon resonances for refractive index sensing applications, *Plasmonics* 8 (2013) 1379–1385.
- [15] T.S. Wu, Y.M. Liu, Z.Y. Yu, Y.W. Peng, C.G. Shu, H.F. He, The sensing characteristics of plasmonic waveguide with a single defect, *Opt. Commun.* 232 (2014) 44–48.
- [16] Y. Peng, J. Hou, Z.H. Huang, Q.S. Lu, Temperature sensor based on surface plasmon resonance within selectively coated photonic crystal fiber, *Appl. Opt.* 51 (26) (2012) 6361–6367.
- [17] S.K. Özdemir, G.T. Sayan, Temperature effects on surface plasmon resonance: design considerations for an optical temperature sensor, *J. Lightwave Technol.* 21 (3) (2003) 805–814 (14).
- [18] T. Kim, K.D. Kihm, Full-field and real-time surface plasmon resonance imaging thermometry, *Opt. Lett.* 32 (23) (2007) 3456–3458.
- [19] H.P. Chiang, H.T. Yeh, C.M. Chen, J.C. Wu, S.Y. Su, R. Chang, Surface plasmon resonance monitoring of temperature via phase measurement, *Opt. Commun.* 241 (2004) 409–418.
- [20] B.F. Yun, G.H. Hu, Y.P. Cui, A nanometric plasmonic waveguide filter based on Fabry-Perot resonator, *Opt. Commun.* 284 (2011) 485–489.
- [21] J.H. Zhu, X.G. Huang, J. Tao, X.P. Jin, X. Mei, Nanometric plasmonic refractive index sensor, *Opt. Commun.* 285 (2012) 3242–3245.
- [22] X.S. Lin, X.G. Huang, Tooth-shaped plasmonic waveguide filters with nanometric sizes, *Opt. Lett.* 33 (23) (2008) 2875–2876.
- [23] D.W. Lynch, W.R. Hunter, Silver (Ag), in: E.D. Palik (Ed.), *Handbook of Optical Constants of Solids*, Academic, Orlando, Fla., 1985.
- [24] S.T. Sundari, K. Srinivasu, S. Dash, A.K. Tyagi, Temperature evolution of optical constants and their tuning in silver, *Solid State Commun.* 167 (2013) 36–39.
- [25] P.X. Chen, R.S. Liang, Q.D. Huang, Y. Xu, Plasmonic filter with sub-waveguide coupled to vertical rectangular resonator structure, *Opt. Commun.* 284 (2011) 4795–4799.
- [26] J.J. Chen, C.W. Sun, Q.H. Gong, Fano resonances in a single defect nanocavity coupled with a plasmonic waveguide, *Opt. Lett.* 39 (1) (2014) 52–55.
- [27] A. Dolatabady, N. Granpayeh, V.F. Nezhad, A nanoscale refractive index sensor in two dimensional plasmonic waveguide with nanodisk resonator, *Opt. Commun.* 300 (2013) 265–268.
- [28] H. Lu, X.M. Liu, L.R. Wang, Y.K. Gong, D. Mao, Ultrafast all-optical switching in nanoplasmonic waveguide with Kerr nonlinear resonator, *Opt. Express* 19 (4) (2011) 2910–2915.
- [29] T.B. Wang, X.W. Wen, C.P. Yin, H.Z. Wang, The transmission characteristics of surface plasmon polaritons in ring resonator, *Opt. Express* 17 (26) (2009) 24096–24101.